Am J Physiol Heart Circ Physiol 293: H2959–H2970, 2007.
First published September 7, 2007; doi:10.1152/ajpheart.00586.2007.

Flow patterns in three-dimensional porcine epicardial coronary arterial tree

Yunlong Huo,[1] Thomas Wischgoll,[2] and Ghassan S. Kassab[1]

[1]*Department of Biomedical Engineering, Surgery, and Cellular and Integrative Physiology, Indiana University Purdue University Indianapolis, Indianapolis, Indiana;* [2]*Department of Computer Science and Engineering, Wright State University, Dayton, Ohio*

Submitted 18 May 2007; accepted in final form 5 September 2007

Huo Y, Wischgoll T, Kassab GS. Flow patterns in three-dimensional porcine epicardial coronary arterial tree. *Am J Physiol Heart Circ Physiol* 293: H2959–H2970, 2007. First published September 7, 2007; doi:10.1152/ajpheart.00586.2007.—The branching pattern of epicardial coronary arteries is clearly three-dimensional, with correspondingly complex flow patterns. The objective of the present study was to perform a detailed hemodynamic analysis using a three-dimensional finite element method in a left anterior descending (LAD) epicardial arterial tree, including main trunk and primary branches, based on computed tomography scans. The inlet LAD flow velocity was measured in an anesthetized pig, and the outlet pressure boundary condition was estimated based on scaling laws. The spatial and temporal wall shear stress (WSS), gradient of WSS (WSSG), and oscillatory shear index (OSI) were calculated and used to identify regions of flow disturbances in the vicinity of primary bifurcations. We found that low WSS and high OSI coincide with disturbed flows (stagnated, secondary, and reversed flows) opposite to the flow divider and lateral to the junction orifice of the main trunk and primary branches. High time-averaged WSSG occurs in regions of bifurcations, with the flow divider having maximum values. Low WSS and high OSI were found to be related through a power law relationship. Furthermore, zones of low time-averaged WSS and high OSI amplified for larger diameter ratio and high inlet flow rate. Hence, different focal atherosclerotic-prone regions may be explained by different physical mechanism associated with certain critical levels of low WSS, high OSI, and high WSSG, which are strongly affected by the diameter ratio. The implications of the flow patterns for atherogenesis are enumerated.

left anterior descending arterial tree; wall shear stress; spatial gradient of wall shear stress; oscillatory shear index

THE CHANGES IN GEOMETRY OF blood vessels during branching can lead to significant flow disturbances (e.g., flow separation, secondary flow, stagnation point flow, reversed flow, and/or turbulence) due to convective inertia (1). These disturbed flows affect various hemodynamic parameters, such as wall shear stress (WSS), WSS spatial gradient (WSSG), and oscillatory shear index (OSI). It has been found that spatial and temporal WSS and WSSG can locally induce abnormal biological response, such as dysfunction of endothelial cells, monocyte deposition, elevated wall permeability to macromolecules, particle migration into the vessel wall, smooth muscle cell proliferation, microemboli formation, and so on (24, 42).

Since the connection between local hemodynamics and endothelial function was made, the computational fluid dynamics (CFD) method has emerged as a powerful tool to study flow patterns in blood vessels (4, 5, 9, 14, 24, 25, 27, 33–36, 39, 40, 46). Perktold et al. (33, 34) compared Newtonian and non-Newtonian unsteady fluid flow in normal carotid arteries using the finite element method (FEM). Kleinstreuer and colleagues (5, 24, 27) studied the relationship between nonuniform hemodynamics at the rabbit aorto-celiac junction. Berger and associates (4, 39) investigated the blood flow with a turbulence model in stenotic vessels. He and Ku (14) and Ku and colleagues (25, 26) solved the pulsatile flow in the human left coronary artery, including the left common coronary artery, left anterior descending (LAD), and left circumflex arteries (LCX). Ramaswamy et al. (35) performed the numerical simulation to study the effects of motion of the coronary artery on the unsteady fluid dynamics. Although the above studies have provided a wealth of simulations on the local flow field in a vessel segment or a bifurcation, a full CFD analysis on a branching tree model based on the measured morphometric data has not been realized.

The objective of the present study is to investigate the pulsatile blood flow in a LAD epicardial arterial tree, including main trunk and primary branches using three-dimensional (3D) FEM. The hemodynamic parameters, such as spatial and temporal WSS, WSSG, and OSI, were analyzed systematically. The results show that high time-averaged WSSG occur in region of bifurcations with the flow divider having the maximum value. Low time-averaged WSS and high OSI obey a power law relationship and coincide with disturbed flows (stagnated, secondary, and reversed flows) opposite to the flow divider and lateral to the junction orifice of the main trunk and primary branches. We conclude that the diameter ratio and inlet flow rate can strongly affect the low WSS, high OSI, and high WSSG, which are important hemodynamic determinants of atherogenesis. The limitations and implications of the novel branching CFD model are contemplated.

MATERIALS AND METHODS

Animal preparation. Studies were performed on five normal Yorkshire porcine of either sex with body weight of 34.3–42.1 kg. The experimental procedures of the animal preparation were similar to those described by Kassab et al. (22). All animal experiments were performed in accordance with national and local ethical guidelines, including the Institute of Laboratory Animal Research guide, Public Health Service policy, Animal Welfare Act, and an approved University of California, Irvine-IACUC protocol.

Briefly, surgical anesthesia was induced with ketamine (33 mg/kg im) and atropine (0.05 mg/kg im) and was maintained with pentobarbital sodium (30 mg/kg iv in an ear vein). A midline sternotomy was performed, ventilation with room air was provided with a respiratory pump, and anticoagulation was provided with heparin (3 mg/kg).

Address for reprint requests and other correspondence: G. S. Kassab, Dept. of Biomedical Engineering, Indiana Univ. Purdue Univ. Indianapolis, Indianapolis, IN 46202 (e-mail: gkassab@iupui.edu).

The costs of publication of this article were defrayed in part by the payment of page charges. The article must therefore be hereby marked "*advertisement*" in accordance with 18 U.S.C. Section 1734 solely to indicate this fact.

Arterial pressure was measured through a catheter inserted through the carotid artery into the ascending aorta and was monitored with a Biopac, MP 100. An incision was made in the pericardium, and the heart was supported in a pericardial cradle. A 1-liter bottle containing a hypothermic (10°C), isotonic, cardioplegic rinsing solution [composed of EGTA, 1 mM; calcium-channel blocker nifedipine, 0.2 mg/l; and adenosine, 80 mg/l] was hung above the heart. A 14-gauge needle was connected to the rinsing solution with Tygon tubing. The needle was inserted into the ascending aorta with no perfusion initially. The heart was then arrested with a saturated KCl solution given through a jugular vein, and the tubing was unclamped to allow immediate perfusion of the cardioplegic rinsing solution. The aorta was clamped proximal to the needle to allow perfusion of the coronaries through Valsalva's sinus. The superior and inferior venae cavae were cut to allow free drainage of blood. The heart was covered with crushed ice for several minutes during perfusion with ~500 ml of cardioplegic solution. The heart was then excised with the ascending aorta still clamped to keep air bubbles out of the coronary arteries.

Anatomical model from computed tomography scan. After the heart was excised, it was placed in a saline solution. The LAD artery, the right coronary artery, and the LCX were cannulated under saline to avoid air bubbles and perfused with cardioplegic solution to flush out the blood. The three major arteries (right coronary artery, LAD, and LCX) were individually perfused at a pressure of 100 mmHg with three different colors of Microfil (Flow Tech). After the Microfil was allowed to harden for 45–60 min, the hearts were kept in the refrigerator in saline solution until the day the computed tomography (CT) scan was performed. The scans were made axially (120 mA, 120 kV, 0.6/0.6 mm slice) on a 16-slice scanner (Siemens Somatom). A reconstructed CT image of LAD arteries, as shown in Fig. 1*a*, was selected for mesh generation.

3D FEM model. The governing equations were formulated for an incompressible, Newtonian fluid in a coronary arterial tree consisting of large epicardial coronary arteries and primary branches, every vessel of which was assumed cylindrical with rigid and

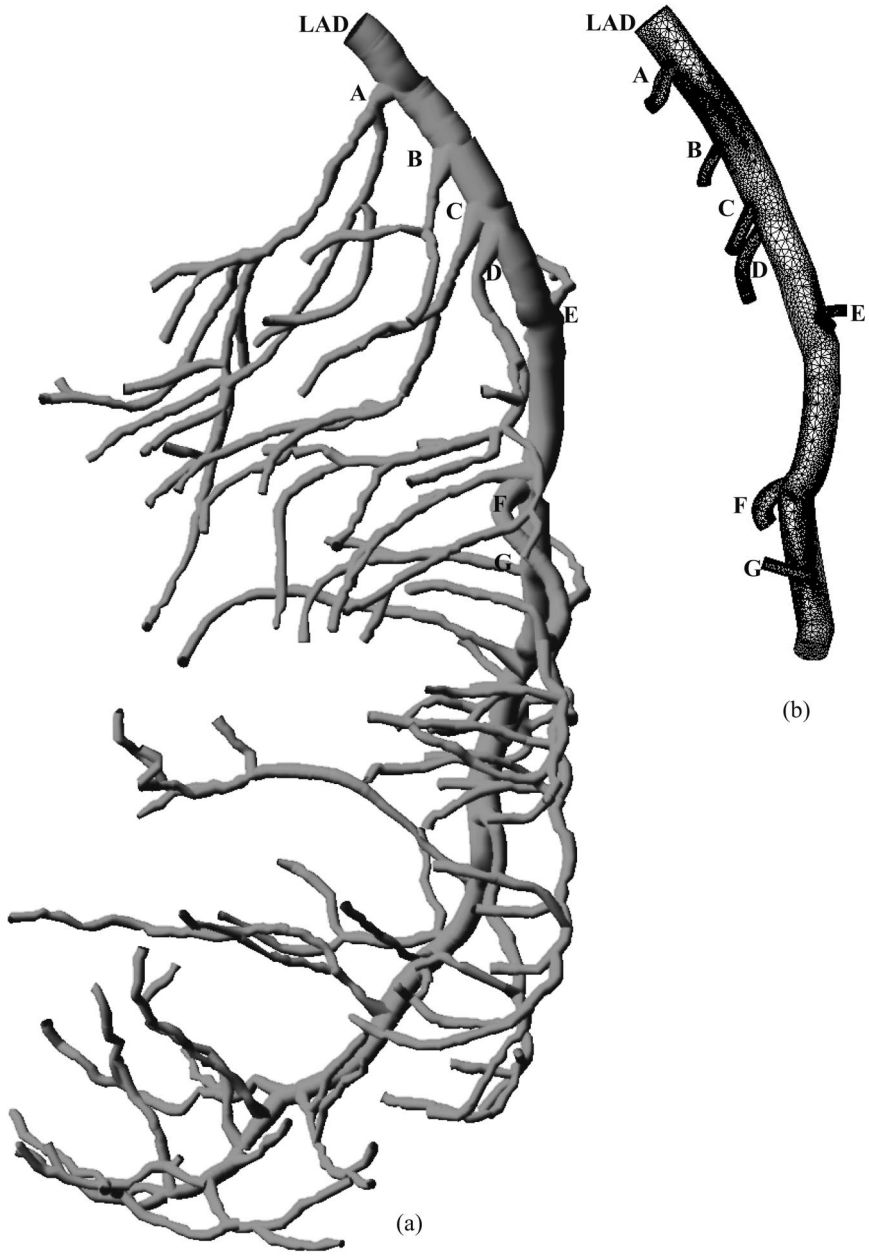

Fig. 1. *a*: Computed tomography scan of porcine left anterior descending (LAD) arterial tree. *b*: Finite element mesh for numerical computation of LAD main trunk (≥2.0 mm in diameter) and primary branches (≥1.0 mm in diameter). *A–G*, branches.

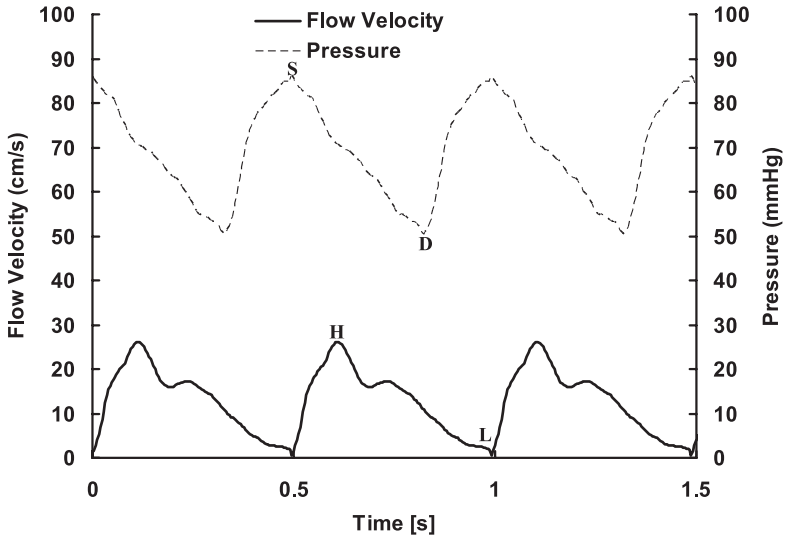

Fig. 2. In vivo pulsatile pressure and flow velocity waveforms measured at the inlet of LAD arterial tree in porcine heart. H and L, high and low instances on the velocity curve, respectively; D, diastole; S, systole. Solid and dash lines represent the flow and pressure waves, respectively.

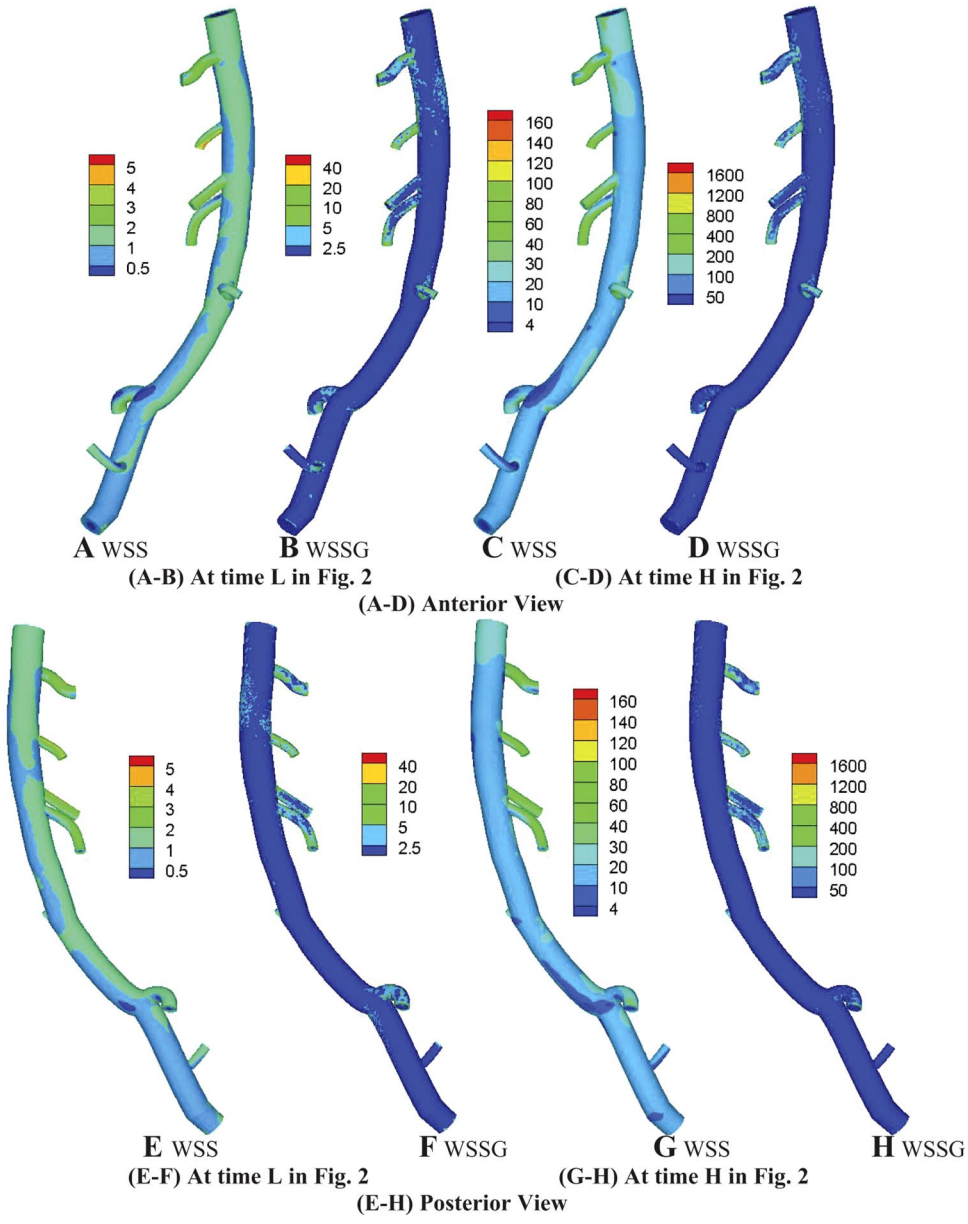

Fig. 3. Distribution of wall shear stress (WSS) (unit: dyn/cm^2) (*A*, *C*, *E*, *G*) and WSS spatial gradient (WSSG) (unit: dyn/cm^3) (*B*, *D*, *F*, *H*) at *time L* (about 1/5 of cardiac cycle after diastolic time; *A*, *B*, *E*, *F*) and *time H* (about 1/5 of cardiac cycle after systolic time; *C*, *D*, *G*, *H*) in anterior view (*A–D*) and posterior view (*E–H*).

impermeable wall. The equations of continuity and Navier-Stokes can be written as:

$$\nabla \cdot \vec{\mathbf{v}} = 0 \quad (1)$$

$$\rho \frac{\partial \vec{\mathbf{v}}}{\partial t} + \rho \vec{\mathbf{v}} \cdot \nabla \vec{\mathbf{v}} = -\nabla P + \nabla \cdot \mu [\nabla \vec{\mathbf{v}} + (\nabla \vec{\mathbf{v}})^T] \quad (2)$$

where $\vec{\mathbf{v}} = u\hat{e}_x + v\hat{e}_y + w\hat{e}_z$ is velocity; P is pressure; ρ is blood mass density; μ is viscosity; and t and T are time. The inlet flow waves shown in Fig. 2 were measured using a Doppler ultrasound probe in an anesthetized animal (2), which served as the inlet boundary condition. The outlet boundary conditions were expressed in terms of pressure waveforms, which were found to have scaling characteristics similar to flow (10). Therefore, the time-averaged outlet pressures were estimated from the scaling relations (23), which can be written as follows:

$$P_{inlet} - P_{outlet} \sim [1 - (D_{outlet}/D_{inlet})^{2\beta-4}] \cdot \Delta P_{max} \quad (3)$$

where P_{inlet} is the inlet pressure; P_{outlet} is the outlet pressure; ΔP_{max} ($= P_{inlet} - P_{capillary}$) is the maximum pressure gradient in the arterial tree; D_{outlet} is outlet diameter; and D_{inlet} is inlet diameter. The coefficient β was found to be 2.1, and the ΔP_{max} was estimated as 50 mmHg. The inlet flow and outlet relative pressure boundary conditions were applied to solve the 3D FEM model. The μ and ρ of the solution were selected as 4 cP and 1.235 g/cm^3, respectively, to mimic the blood flow in large epicardial arteries.

Numerical method. The transient equations of fluid flow were solved using ANSYS commercial software. The smart size was applied to the Fluid 142 elements, which provide reasonably shaped elements during automatic mesh generation (e.g., the concentration of mesh is implemented at bifurcations and small vessels). A tetrahedral-shaped element is formed by appropriately combining the nodes in a brick element. Before the final simulation, a mesh dependency was conduced so that the relative error in two consecutive mesh refinements was smaller than 1% for the maximum velocity for steady-state flow with inlet flow velocity equal to the time-averaged velocity over a cardiac cycle. A total of almost 500,000 finite elements was required to accurately mesh the computational domains. The final mesh used for the computations is shown in Fig. 1*b* for the numerical computation of LAD main trunk and primary branches, where the diameter and length of the LAD trunk (down to 2.0 mm in diameter) and primary branches (larger than >1.0 mm) were selected. The backward method was used for the time integration. A constant time step was employed, where $\Delta t = 0.004$ s with 124 total time step per cardiac cycle. At each time step, convergence criteria of 1×10^{-4} and 1×10^{-12} were set for relative error associated with determination of velocity and pressure, respectively. Three cardiac cycles were required to achieve convergence for the transient analysis. Using duo processors of Precision 670, the total central processing unit time was ~60 h for each simulation case.

Hemodynamic parameters. The velocity and pressure of the blood flow were calculated by solving the equations of continuity and Navier-Stokes. Reynolds, Womersley, and Dean numbers were obtained from the geometry and dynamic results. WSS, WSSG, and OSI were determined based on the velocity field (see detailed formulation in APPENDIX).

RESULTS

The branching FEM model was used to compute the distribution of pulsatile blood flow in the main trunk and primary branches of the LAD arterial tree. Numerical simulations were carried out for various parameters and com-

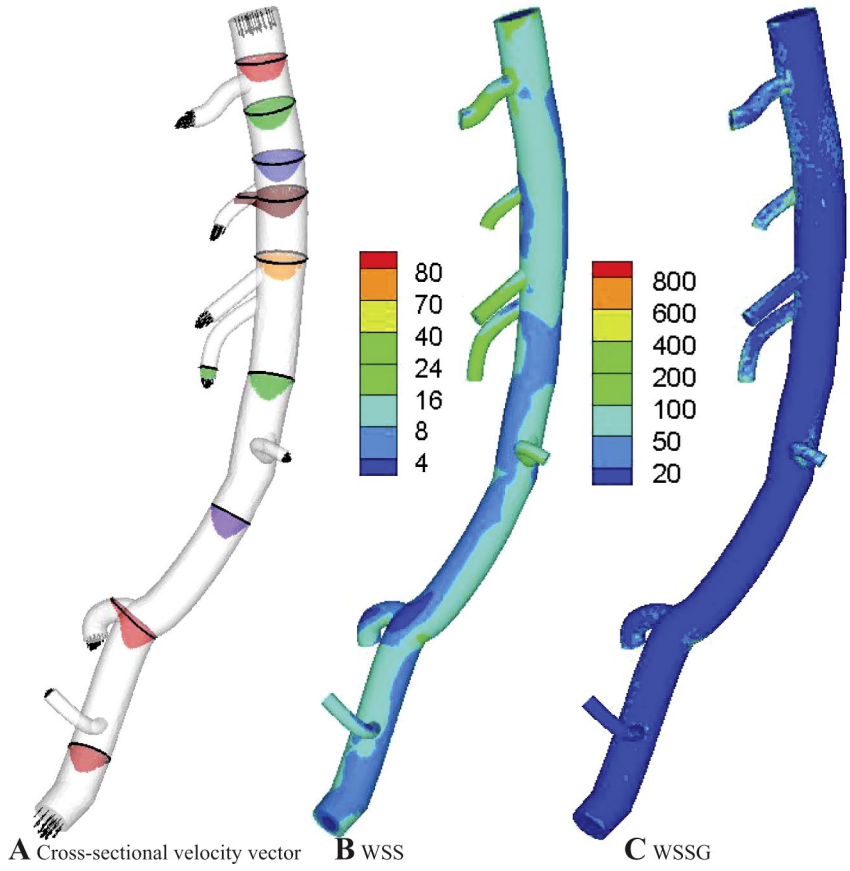

Fig. 4. Time-averaged velocity vector (grid units/magnitude of velocity = 0.0085; *A*), WSS (unit: dyn/cm^2; *B*), and WSSG (unit: dyn/cm^3; *C*) fields over a cardiac cycle in anterior view.

putational domains. A selection of numerical results is given below.

Flow in LAD artery trunk. The reconstructed CT image in Fig. 1*a* is discretized into meshes, as shown in Fig. 1*b*, for implementing the FEM simulation with a blunt core velocity profile at the inlet of the LAD tree with the temporal profile given in Fig. 2. Reynolds numbers are 14 and 229 at velocity wave trough and crest time points (*time points L* and *H* in Fig. 2, which are about one-fifth of the cardiac cycle after diastolic or systolic instance), respectively, and the corresponding Dean numbers are about 18 and 277 in the main trunk of the LAD epicardial arterial tree. Figure 3 shows the distribution of WSS (unit: dyn/cm^2) and WSSG (unit: dyn/cm^3) at velocity wave trough and crest time points in anterior and posterior views, respectively. It is observed that high flow rates at the inlet of the LAD artery induce high WSS (Fig. 3, *C* and *G*) and WSSG (Fig. 3, *D* and *H*) along the blood vessel wall, respectively, and vice versa. Zones of low WSS are found to enlarge from trough to crest time points.

Figure 4*A* shows the time-averaged cross-sectional flow velocity vector over a cardiac cycle. The Reynolds and Dean numbers averaged over a cardiac cycle and Womersley number are approximately equal to 110, 132, and 3, respectively, in the main trunk of the LAD artery. It is found that the blunt core velocity profile at the inlet of LAD is developed into a parabolic velocity profile (fully developed Hagen-Poiseuille velocity profile) at ~2.2 cm from the inlet of LAD. The fully developed parabolic profile is distorted at the bifurcation of the main trunk and primary branches. The mean flow velocity over the cross-sectional area of the main trunk remains uniform, since the relative errors are within ±10%. Figure 4, *B* and *C*, shows the distribution of time-averaged WSS and WSSG over a cardiac cycle, respectively. It is found that WSS distribution is complex near bifurcations of the main trunk and primary branches. In particular, Figs. 3 and 4 depict that the values of WSSG near bifurcations are much higher than those of other sites. Therefore, the fluid flow in the vicinity of bifurcations is further explored because of the complex flow patterns.

Flow near bifurcations. Because primary *branches A–D* in Fig. 1*b* have similar diameter ratio to the main trunk (D_{pb}/D_m is approximately equal to 0.33, where D_{pb} and D_m

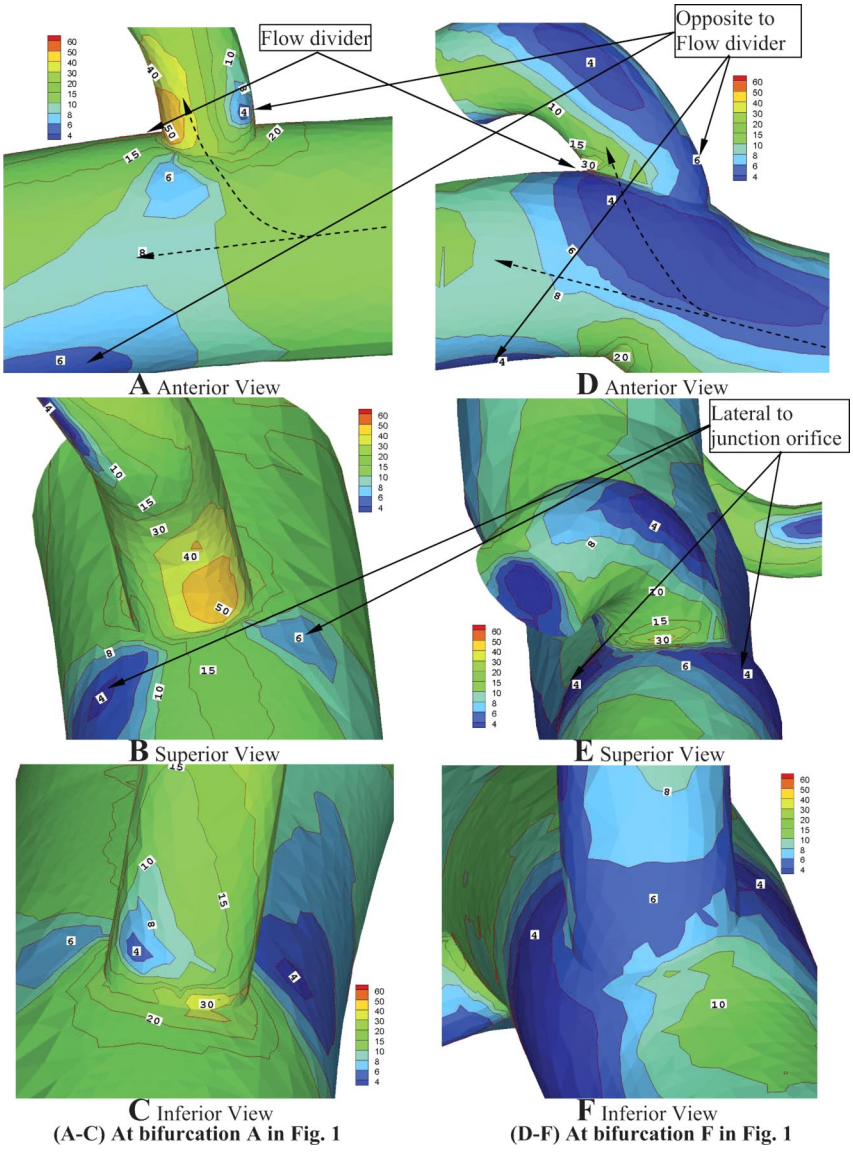

Fig. 5. *A–C*: time-averaged WSS (unit: dyn/cm^2) distribution at bifurcations (*primary branch A* in Fig. 1*b*) over a cardiac cycle in anterior, superior, and inferior view, respectively. *D–F*: time-averaged WSS (unit: dyn/cm^2) distribution at bifurcations (*primary branch F* in Fig. 1*b*) over a cardiac cycle in anterior, superior, and inferior view, respectively. *A* and *D*: dash lines represent the flow direction in main trunk and primary branches.

are the diameters of primary branch and mother vessel in main trunk, respectively), *branch A* was selected for further analysis. Compared with primary *branch A*, *branch F* with larger diameter ratio (D_{pb}/D_m is equal to 0.71) was used to investigate the effect of diameter ratio. Figure 5, *A–C* and *D–F*, shows the time-averaged WSS (unit: dyn/cm^2) distribution at bifurcations (primary *branches A* and *F*, respectively, in Fig. 1*b*) over a cardiac cycle from various view points. It is found that high (>30 dyn/cm^2) and low time-averaged WSS (<6 dyn/cm^2) occur near the flow divider (defined as the anastomosis at the downstream wall of the primary branch proximal to the main trunk, as shown in Fig. 5) and opposite to the flow divider, respectively. There are two areas opposite the flow divider: one in the primary branches and the other in the main trunk, as shown in Fig. 5, *A* and *D*. Low WSS is approximately crescent-shaped. There are two important areas with low WSS in the wall of the main trunk lateral to the junction orifice of the main trunk and primary branches. Comparison of Fig. 5, *A–C* with *D–F* shows that zones of low WSS are enlarged for a larger diameter ratio. It should be noted that low WSS is not exactly opposite to the flow divider.

In correspondence to Fig. 5, *A–F*, Fig. 6, *A–F*, shows the respective OSI distribution at bifurcations over a cardiac cycle. It is found that low WSS approximately coincides with high OSI, which approximately obeys a power law relation. Table 1 lists the exponent (β) and correlation coefficient for the power law relation (OSI $\sim$ WSS$^{\beta}$) lateral to the junction orifice and opposite to the flow divider near *bifurcations A–G* in Fig. 1*b*. Furthermore, Fig. 7 shows the time-averaged WSSG (unit: dyn/cm^3) distribution at previously cited bifurcations over a cardiac cycle. High time-averaged WSSG is found in the region of bifurcations and has a relatively large value near the flow divider, which coincides with high WSS zones. Table 2 lists the relationship between hemodynamic parameters (i.e., WSS, OSI, and WSSG) and atherosclerotic-prone region in the main trunk and primary branches of the LAD epicardial arterial tree.

Figure 8, *A–C* and *D–F*, shows the distribution of time-averaged flow velocity vectors (grid units/magnitude of velocity = 0.005) in various planes at *bifurcations A* (*A–C*) and *F* (*D–F*), respectively, over a cardiac cycle. Figure 9, *A–F*, shows the corresponding distribution of flow velocity vectors (grid

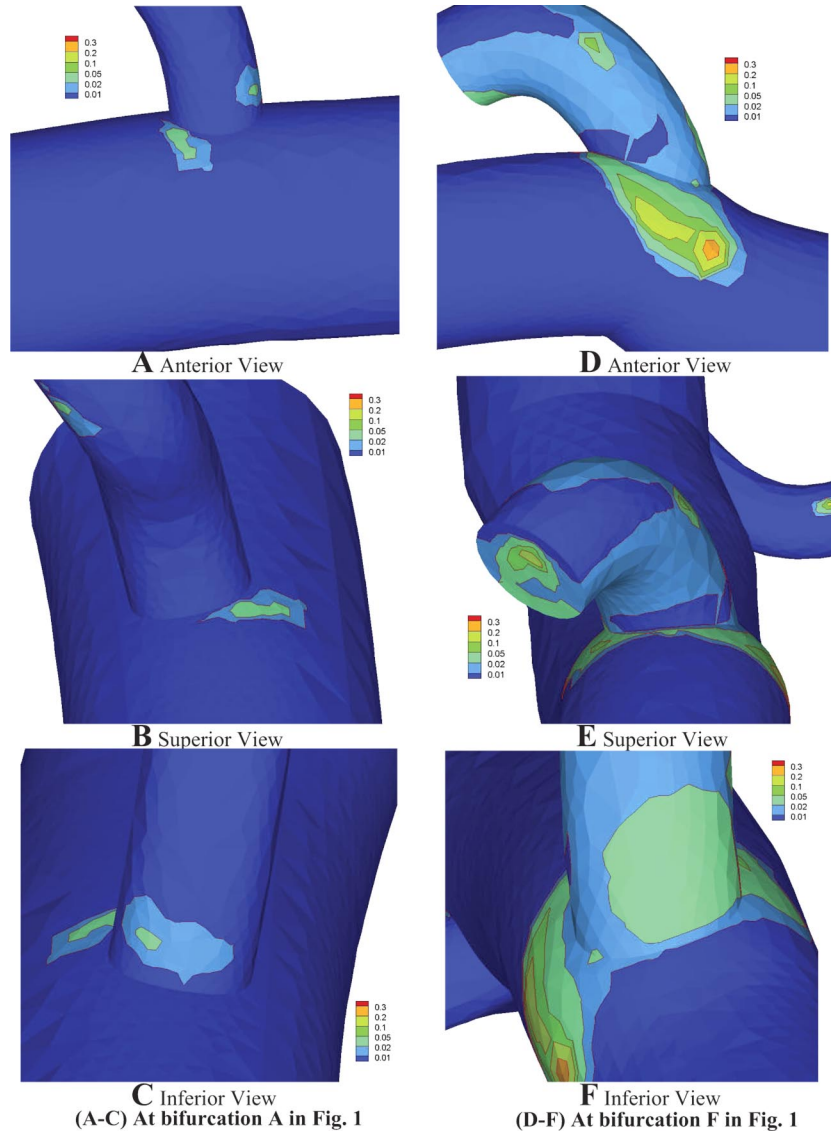

Fig. 6. Oscillatory shear index distribution at bifurcations over a cardiac cycle. *A–F* correspond to Fig. 5, *A–F*, respectively.

Table 1. *Exponent β and correlation coefficient R^2 for the power law relation (OSI ~ WSS$^{\beta}$) lateral to the junction orifice and opposite to the flow divider near bifurcations, where high OSI coincides with low WSS*

Position	β	R^2
Opposite to the flow divider (in primary branches)		
Bifurcation A	−0.68	0.53
Bifurcation B	−1.70	0.75
Bifurcation C	−1.64	0.50
Bifurcation D	−1.63	0.64
Bifurcation E	N/A	N/A
Bifurcation F	−3.86	0.63
Bifurcation G	N/A	N/A
Lateral to the junction orifice (in main trunk)		
Bifurcation A	−1.40	0.48
Bifurcation B	−2.88	0.59
Bifurcation C	−1.02	0.44
Bifurcation D	−1.35	0.45
Bifurcation E	N/A	N/A
Bifurcation F	−1.82	0.63
Bifurcation G	−0.84	0.43

N/A, not applicable, because the value of oscillatory shear index (OSI) is very small ($<10^{-3}$), which implies that there is no significant disturbed flow in the region of bifurcation. WSS, wall shear stress.

units/magnitude of velocity = 0.05) at diastole (*time instance D* in Fig. 2). The disturbed flows (stagnated, secondary, and reversed flows) are found in Figs. 8 and 9. The time-averaged flow velocity in zones of low WSS is apparently smaller than zones of high WSS, as shown in Fig. 8. The secondary and reversed flows appear near *bifurcations F* and *A*, as shown in Fig. 9, *E* and *B*, respectively, at diastole. Furthermore, it is found that the flow in primary branches changes gradually from forward to reverse flow during the diastolic period (i.e., from *time points S* to *D* in Fig. 2).

DISCUSSION

Since Fry (12) and Caro et al. (6) proposed that high and low WSS, respectively, affect atherogenesis, a large number of studies (1–15, 24–30, 32–46) have been carried out. In the present study, we used 3D FEM model to perform a detailed hemodynamic analysis, based on geometry from CT scans and experimentally measured boundary conditions in the LAD epicardial arterial tree. We report several major findings, including the following: *1*) low time-averaged WSS and high OSI approximately obey a power law relation, which coincides with disturbed flows opposite to the flow divider and lateral to the junction orifice; *2*) zones of low time-averaged WSS and high OSI amplify at higher flow rates at the inlet of LAD and with larger diameter ratio; and *3*) high time-averaged WSSG was found in region of bifurcations with the maximum value at the flow divider. We will elaborate on each of these findings below.

Flow in LAD artery trunk. In Fig. 4*A*, the blunt profile became a fully developed parabolic profile at ~2.2 cm, which is consistent with the theoretical development length, L [$= D \times (0.06 \times \mathrm{Re}) = 2.24$], where D is the LAD inlet diameter and Re is Reynolds number. Reynolds (inertial force/viscous force) and Dean (D_n = centrifugal force/viscous force) numbers increased when the velocity wave changed from trough to crest time points (from *time L* to *H* in Fig. 2). In the main trunk of the LAD epicardial arterial tree of an anesthetized pig, Reynolds and Dean numbers in trough and crest instance were in the regime where the viscous forces are dominant over centrifugal forces. Hence, there is no instability or strong separation caused by the curvature of the main trunk (31, 32). The uniformity of mean flow velocity in the main trunk is consistent with previous predictions (21).

The WSS at velocity wave trough, average, and crest time (see Figs. 3*A*, 4*B*, and 3*C*, respectively) showed that zones of low WSS amplified when flow rates at the inlet of LAD increased during the cardiac cycle. The locations of low WSS are consistent with the experimental results of fluid flow in the LAD epicardial tree by Asakura and Karino (1). The high time-averaged WSSG (in Fig. 4*C*) was found in the region of bifurcations, with the flow divider having the maximum value. This agrees with the numerical results in the normal left coronary arterial tree by Framakis et al. (9) and at the rabbit aorto-celiac junction by Buchanan et al. (5).

Flow near bifurcations. Many researchers (1, 4–6, 9–11, 14, 15, 26, 27, 30, 33–36, 39, 40, 44–46) have found that atherosclerosis is a geometrically focal disease that has a propensity to involve the outer edges of blood vessel bifurcations, where low WSS (see Ref. 29) is prevalent. Furthermore, high WSSG (5, 7–8, 15, 27, 45) has been implicated in the site of elevated low density lipoprotein permeability and lesion growth, such as the flow divider. Here, we investigated these two hemodynamic factors.

WSS and OSI. Bifurcations represent complex local geometric changes and correspondingly complex flow. The low WSS in the wall opposite to the flow divider and lateral to the junction orifice in Fig. 5 can strongly affect endothelial cell morphology and functions. For example, endothelial proliferation and apoptosis can be elevated in low WSS (see Refs. 29, 42). The temporal gradient of WSS is also important to stimulate endothelial cell proliferation (3, 43). In the present study, OSI (14, 26) was used to quantify the temporal gradient of WSS. Since OSI does not differentiate between flow separation and general flow disturbance (24), it was only considered along the wall of the LAD epicardial arterial tree. The high OSI (in Fig. 6) was found to coincide with the low WSS in the wall of primary branches opposite to the flow divider and main trunk lateral to the junction orifice, which followed a power law relationship (Table 1). There was no high OSI, however, in the wall of the main trunk opposite to the flow divider in Fig. 6, *A* and *D*. Figure 9 shows strong secondary and reversed flow in the wall of primary branches opposite to the flow divider and main trunk lateral to the junction orifice, but not in the wall of the main trunk opposite to the flow divider. Therefore, secondary and reversed flows near the wall of vessels result in high OSI. Our laboratory's previous findings (28) showed that nitric oxide was reduced during reversed flow, which could lead to vascular dysfunction, including intimal hyperplasia, cell activation, and platelet adhesion. Therefore, atherosclerotic-prone area may be realized in zones of low WSS or high OSI.

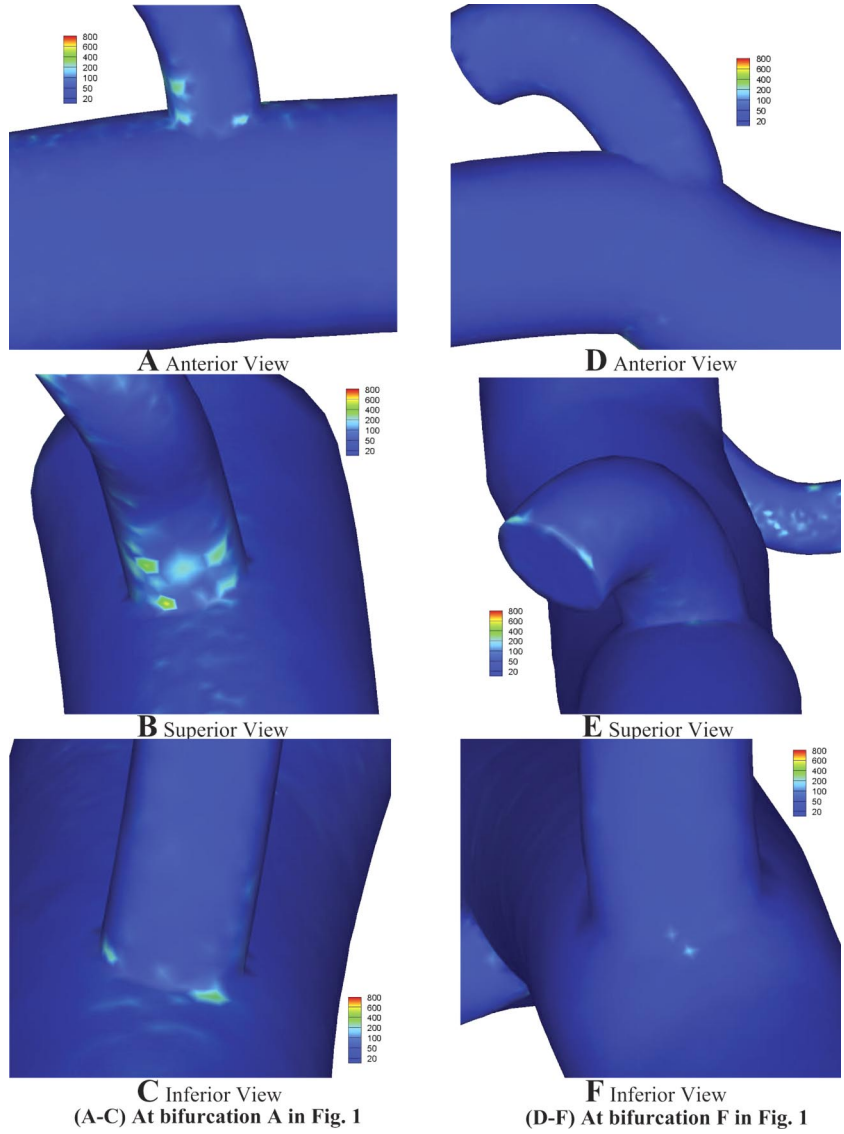

Fig. 7. Time-averaged WSSG (unit: dyn/cm^3) at bifurcations over a cardiac cycle. *A–F* correspond to Fig. 5, *A–F*, respectively.

To explore the flow at bifurcations, we investigated primary branches with different diameter ratios (e.g., primary *branches A–D* and *F*). Zones of low WSS enlarged with larger diameter ratio (comparison of Fig. 5, *A* and *D*), while the mean flow velocity in the main trunk remained uniform. Our previous study (16) indicates that branching angles are smaller with larger diameter ratios. The large diameter ratio and small branching angles can induce complex flow patterns in larger area of the main trunk and primary branches and further enlarge zones of low WSS. For example, the carotid artery bifurcation (39) with larger diameter ratio has much more complex flow patterns than the LAD arterial tree. High OSI can be found in the wall of the main trunk opposite to the flow divider when the diameter ratio is sufficiently large, such as the carotid artery bifurcation (39). This novel finding makes a connection between diameter ratio and possible atherosclerotic lesions.

WSSG. DePaola et al. (8) postulated that high WSSG induce morphological and functional changes in endothelium. Herrmann et al. (15) and Zeindler et al. (45) showed

Table 2. *Relationship between hemodynamic parameters and atherosclerotic-prone region in main trunk and primary branches of LAD epicardial arterial tree*

Hemodynamic Parameters	Atherosclerotic-Prone Region in Main Trunk	Atherosclerotic-Prone Region in Primary Branches
Low WSS	Lateral to the junction orifice and opposite to the flow divider	Opposite to the flow divider
High OSI	Lateral to the junction orifice	Opposite to the flow divider
High WSSG	Flow divider	Flow divider

WSSG, wall shear stress gradient.

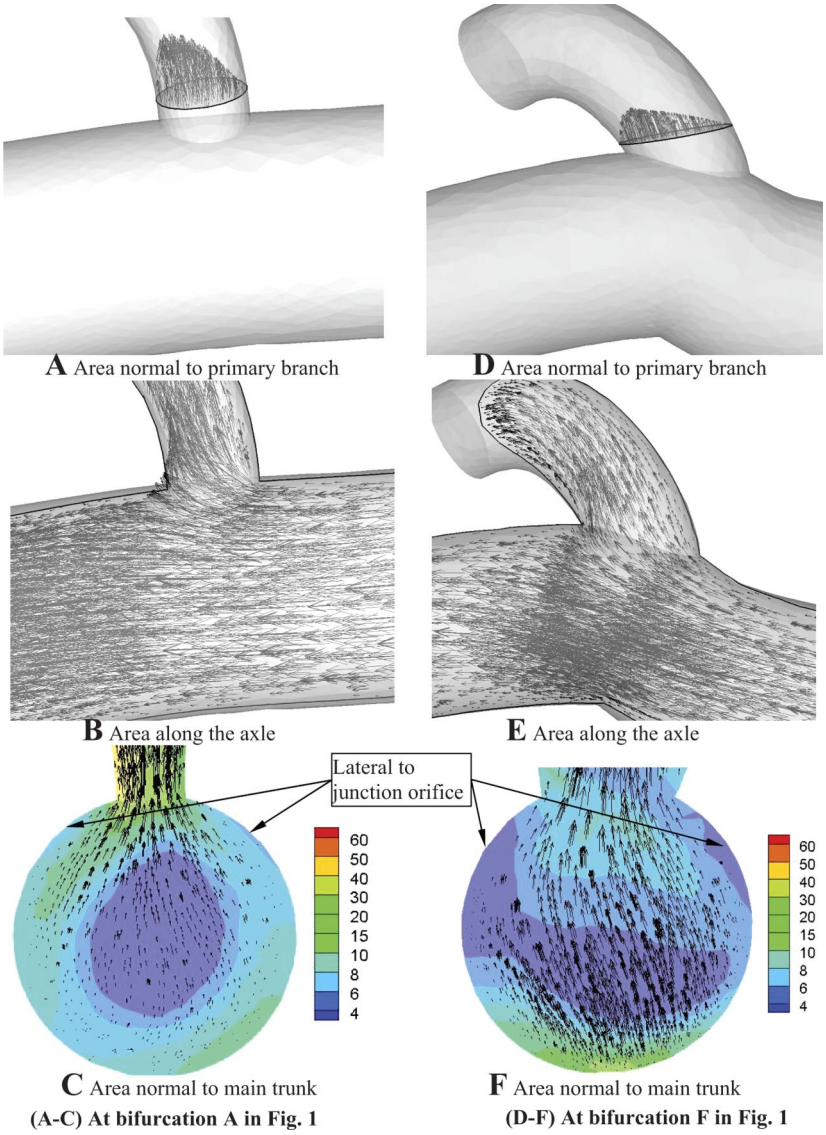

Fig. 8. Distribution of time-averaged flow velocity vectors (grid units/magnitude of velocity = 0.005) in the sectioned area at *bifurcations A* (*A–C*) and *F* (*D–F*) over a cardiac cycle. The colorful plots in *C* and *F* represent the distribution of WSS (unit: dyn/cm^2).

elevated permeability and lesion growth at the flow divider, where WSSG is high and WSS is low. Kleinstreuer and colleagues (5, 27) used elevated WSSG to explain the experimental observation by Herrmann et al. (15) and Zeindler et al. (45). They indicated that the highest low-density lipoprotein permeability and largest sites of elevated permeability are associated with zones of elevated WSSG. In the present study, our findings of WSSG (in Fig. 7) in the LAD epicardial arterial tree are consistent with Kleinstreuer's results.

Other researchers (9) studied WSSG in the normal LAD epicardial tree and postulated that low WSSG correlates with atherosclerosis locations. As shown in Fig. 4*C*, most sites have low WSSG, except for small regions near bifurcations. Hence, low WSSG may not be the cause of atherosclerosis as such extensive lesions have not been observed clinically. The locations of high WSSG, however, are a good candidate for focal atherosclerosis.

Comparison with other models. Buchanan et al. (5) compared the spatial distribution of the WSS, WSSG, and OSI with the experimental measurements of Herrmann et al. (15) and Zeindler et al. (45) at the rabbit aorto-celiac junction. Compared with the rabbit aorto-celiac junction (see Figs. 3–6 in Ref. 5), Figs. 5–7 show similar distribution of hemodynamic parameters in LAD epicardial arterial tree. Although different sites in the cardiovascular system are considered, the same distribution of hemodynamic parameters persists. This suggests that the stimuli for focal atherosclerotic-prone regions may be ubiquitous in the cardiovascular system and relate to critical levels of low WSS, high OSI, and high WSSG, which are strongly affected by diameter ratio.

Critique of the model. Although our simulation is based on real geometry (from CT scans) and measured inlet flow rate, the elastic wall was simplified to be rigid, and the spatial movement of the vessel wall was neglected. Furthermore, only a portion of the LAD epicardial arterial tree was included in the present 3D model. When detailed data on elasticity, permeability, and cardiac motion are available, they can be implemented by combining the present model and previous studies (16–23).

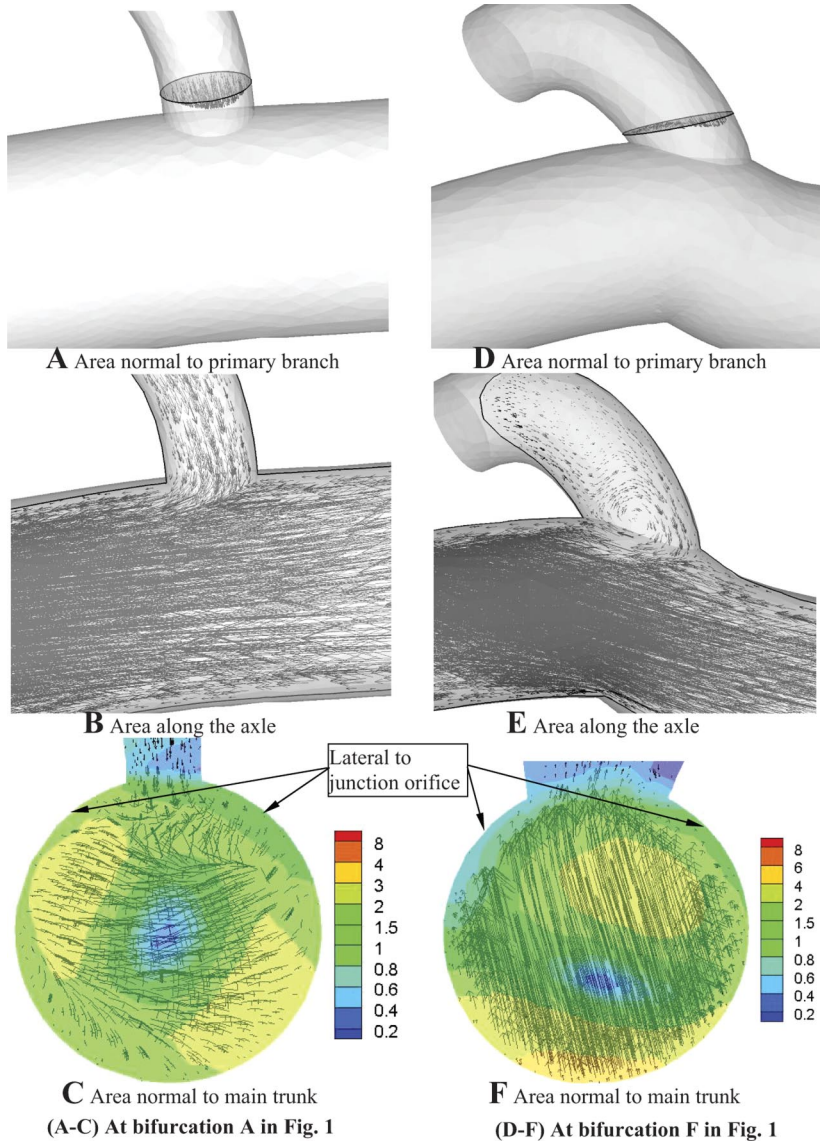

Fig. 9. Distribution of flow velocity vectors (grid units/magnitude of velocity = 0.05) in the sectioned area at diastolic time (*time instance D* in Fig. 2). *A–F* correspond to Fig. 8, *A–F*. The colorful plots in *C* and *F* represent the distribution of WSS (unit: dyn/cm^2).

Significance of study. The present study used a 3D FEM model to analyze the detailed flow patterns in the LAD epicardial arterial tree. We considered the WSS, OSI, and WSSG for bifurcations of different diameter ratios, as these parameters affect endothelial biology. A power law relation between WSS and OSI was found in the wall of primary branches opposite to the flow divider and main trunk lateral to the junction orifice. The atherosclerotic-prone regions (e.g., flow divider, opposite to flow divider, lateral to junction orifice, etc.) were associated with low WSS, high OSI, and high WSSG. Several novel findings emerged, which relate atherosclerotic-prone regions to the diameter ratio and flow. The model will ultimately be made patient specific, which can provide quantitative hemodynamic information to help cardiologist and cardiovascular surgeons select appropriate treatment. This approach will significantly contribute to diagnostic, therapeutic, and treatment design.

APPENDIX

Hemodynamic Parameters

The Reynolds (Re), Womersley (α), and Dean numbers (D_n) are defined, respectively, in the main trunk of the LAD epicardial arterial tree as follows:

$$\mathrm{Re} = \frac{\rho V \cdot D}{\mu} \qquad (A1)$$

$$\alpha = R\sqrt{\frac{\omega\rho}{\mu}} \qquad (A2)$$

$$D_n = \left(2\frac{R}{R_{curve}}\right)^{1/2} \cdot 4\mathrm{Re} \qquad (A3)$$

where $V = V_{min}$, V_{max}, or V_{mean} is minimum, maximum, or time-averaged velocity at the inlet of LAD arterial tree, respectively; R is radius of LAD; D is diameter of LAD, ω is angular

frequency of beating hearts; ρ is blood mass density; and μ is viscosity.

At any point of 3D FEM model, the stress can be represented as a nine-component tensor ($\bar{\bar{\tau}}$), which can be written as follows:

$$\bar{\bar{\tau}} = \begin{bmatrix} \tau_{11} & \tau_{12} & \tau_{13} \\ \tau_{21} & \tau_{22} & \tau_{23} \\ \tau_{31} & \tau_{32} & \tau_{33} \end{bmatrix} = 2\mu\bar{\bar{D}} = \mu \begin{bmatrix} 2\frac{\partial u}{\partial x} & \frac{\partial u}{\partial y}+\frac{\partial v}{\partial x} & \frac{\partial u}{\partial z}+\frac{\partial w}{\partial x} \\ \frac{\partial u}{\partial y}+\frac{\partial v}{\partial x} & 2\frac{\partial v}{\partial y} & \frac{\partial v}{\partial z}+\frac{\partial w}{\partial y} \\ \frac{\partial u}{\partial z}+\frac{\partial w}{\partial x} & \frac{\partial v}{\partial z}+\frac{\partial w}{\partial y} & 2\frac{\partial w}{\partial z} \end{bmatrix} \quad (A4)$$

where $\bar{\bar{D}} = 0.5\cdot[(\nabla\mathbf{v}) + (\nabla\mathbf{v})^T]$ is the shear rate tensor. The stress on the wall, its normal component, and it two tangential components can be written as, respectively:

$$\vec{\tau} = \bar{\bar{\tau}}\cdot\mathbf{n}, \quad \tau_n = \mathbf{n}\cdot\bar{\bar{\tau}}\cdot\mathbf{n}, \quad \tau_{t_1} = \mathbf{t}_1\cdot\bar{\bar{\tau}}\cdot\mathbf{n}, \quad \text{and} \quad \tau_{t_2} = \mathbf{t}_2\cdot\bar{\bar{\tau}}\cdot\mathbf{n} \quad (A5)$$

where $\mathbf{n}$, $\mathbf{t}_1$, and $\mathbf{t}_2$ are the unit vector in the normal and two tangential directions, respectively. The present time-averaged OSI can be written as follows:

$$\mathrm{OSI} = \frac{1}{2}\left(1 - \frac{\left|\frac{1}{T}\int_0^T \vec{\tau}\right|}{\frac{1}{T}\int_0^T |\vec{\tau}|}\right) \quad (A6)$$

The spatial derivatives of the stress can be obtained as follows:

$$\nabla\vec{\tau} = \begin{bmatrix} \frac{\partial\tau_n}{\partial n} & \frac{\partial\tau_n}{\partial t_1} & \frac{\partial\tau_n}{\partial t_2} \\ \frac{\partial\tau_{t_1}}{\partial n} & \frac{\partial\tau_{t_1}}{\partial t_1} & \frac{\partial\tau_{t_1}}{\partial t_2} \\ \frac{\partial\tau_{t_2}}{\partial n} & \frac{\partial\tau_{t_2}}{\partial t_1} & \frac{\partial\tau_{t_2}}{\partial t_2} \end{bmatrix} \quad (A7)$$

where n, t_1, and t_2 are the natural coordinates as shown. As define by Ref. 27, the diagonal components $\partial\tau_{t_1}/\partial t_1$ and $\partial\tau_{t_2}/\partial t_2$ generate intracellular tension, which causes widening and shrinking of cellular gap. However, the diagonal component $\partial\tau_n/\partial n$ can cause endothelial cells rotation, which may destroy the endothelial function too. Therefore, we defined the WSSG as follows:

$$\mathrm{WSSG} = \left[\left(\frac{\partial\tau_n}{\partial n}\right) + \left(\frac{\partial\tau_{t_1}}{\partial t_1}\right) + \left(\frac{\partial\tau_{t_2}}{\partial t_2}\right)\right]^{\frac{1}{2}} \quad (A8)$$

The time-averaged WSSG can be written:

$$\text{time-averaged WSSG} = \frac{1}{T}\int_0^T \mathrm{WSSG}\cdot\mathrm{d}t \quad (A9)$$

To plot the shear stress in the entire computational domain, WSS is determined as the product of viscosity (μ) and wall shear rate ($\dot{\gamma}$), which is defined as:

$$\mathrm{WSS} = \mu\dot{\gamma} = \mu\left\{\begin{array}{l} 2\left[\left(\frac{\partial u}{\partial x}\right)^2 + \left(\frac{\partial v}{\partial y}\right)^2 + \left(\frac{\partial w}{\partial z}\right)^2\right] + \left[\left(\frac{\partial u}{\partial y}\right)^2 + \left(\frac{\partial v}{\partial x}\right)^2\right] \\ \quad + \left[\left(\frac{\partial v}{\partial z}\right)^2 + \left(\frac{\partial w}{\partial y}\right)^2\right] + \left[\left(\frac{\partial w}{\partial x}\right)^2 + \left(\frac{\partial u}{\partial z}\right)^2\right] \end{array}\right\} \quad (A10)$$

The time-averaged WSS and OSI can be written as follows:

$$\text{time-averaged WSS} = \frac{1}{T}\int_0^T \mathrm{WSS}\cdot\mathrm{d}t \quad (A11)$$

Equations A6 and *A8–A11* were used to calculate the OSI, WSSG, and WSS in the FEM model. In the FORTRAN program, we calculated the shear stress, spatial gradient of shear stress, and OSI for each FEM node. However, the values for WSS, WSSG, and OSI were only considered on the endothelial surface of vessels.

ACKNOWLEDGMENT

We thank Charles Dang for providing the experimental flow data.

GRANTS

This research is supported in part by National Heart, Lung, and Blood Institute Grant 2 R01 HL055554-11.

REFERENCES

1. **Asakura T, Karino T.** Flow patterns and spatial distribution of atherosclerotic lesions in human coronary arteries. *Circ Res* 66: 1045–1066, 1990.
2. **Axelsson M, Dang Q, Pitsillides K, Munns S, Hicks J, Kassab GS.** A novel fully implantable multi-channel biotelemetry system for measurement of blood flow, pressure, ECG and temperature. *J Appl Physiol* 102: 1220–1228, 2007.
3. **Bao X, Lu C, Frangos JA.** Mechanism of temporal gradients in shear-induced ERK1/2 activation, and proliferation in endothelial cells. *Am J Physiol Heart Circ Physiol* 281: H22–H29, 2001.
4. **Berger SA, Jou LD.** Flows in stenotic vessels. *Annu Rev Fluid Mech* 32: 347–382, 2002.
5. **Buchanan JR Jr, Kleinstreuer C, Truskey GA, Ming L.** Relation between non-uniform hemodynamics and sites of altered permeability and lesion growth at the rabbit aorto-celiac junction. *Atherosclerosis* 143: 27–40, 1999.
6. **Caro CG, Fitz-Gerald JM, Schroter RC.** Atheroma and arterial wall shear observations, correlation and proposal of a shear dependent mass transfer mechanism for atherogenesis. *Proc R Soc Lond B Biol Sci* 177: 109–159, 1971.
7. **Davies PF, Remuzzi A, Gordon EJ, Dewey CF Jr, Gimbrone MA Jr.** Turbulent fluid shear stress induces vascular endothelial cell turnover in vitro. *Proc Natl Acad Sci USA* 83: 2114–2117, 1986.
8. **DePaola N, Gimbrone MA, Davies PF, Dewey CF.** Vascular endothelium response to fluid shear stress gradients. *Arterioscler Thromb Vasc Biol* 12: 1254–1257, 1993.
9. **Farmakis TM, Soulis JV, Giannoglou GD, Zioupos GJ, Louridas GE.** Wall shear stress gradient topography in the normal left coronary arterial tree: possible implications for atherogenesis. *Curr Med Res Opin* 20: 587–596, 2004.
10. **Friedman MH, Hutchins GM, Bargeron CB, Deters DJ, Mark FF.** Correlation between intimal thickness and fluid shear in human arteries. *Atherosclerosis* 39: 425–436, 1981.
11. **Friedman MH, Bargeron CB, Deters DJ, Mark FF, Hutchins GM.** Correlation between wall shear and intimal thickness at a coronary artery branch. *Atherosclerosis* 68: 27–33, 1987.
12. **Fry DL.** Acute vascular endothelia changes associated with increased blood velocity gradients. *Circ Res* 22: 165–197, 1968.
13. **Glagov S, Zarins CK.** Is intimal hyperplasia an adaptive response or a pathologic process? Observation on the nature of nonatherosclerotic intimal thickening. *J Vasc Surg* 10: 571–573, 1989.
14. **He X, Ku DN.** Pulsatile flow in the human left coronary artery bifurcation: average conditions. *J Biomech Eng* 118: 74–82, 1996.
15. **Herrmann RA, Malinauskas RA, Truskey GA.** Characterization of sites of elevated low density lipoprotein at the intercostals celiac, and iliac branches of the rabbit aorta. *Arterioscler Thromb Vasc Biol* 14: 313–323, 1994.
16. **Huo Y, Kassab GS.** A hybrid one-dimensional/Womersley model of pulsatile blood flow in the entire coronary arterial tree. *Am J Physiol Heart Circ Physiol* 292: H2623–H2633, 2007.
17. **Huo Y, Kassab GS.** Capillary perfusion and wall shear stress are restored in the coronary circulation of hypertrophic right ventricle. *Circ Res* 100: 273–283, 2007.

18. **Huo Y, Kassab GS.** Pulsatile blood flow in the entire coronary arterial tree: theory and experiment. *Am J Physiol Heart Circ Physiol* 291: H1074–H1087, 2006.
19. **Huo Y, Li BQ.** Surface deformation and marangoni convection in electrostatically-positioned droplets of immiscible liquids under microgravity. *ASME J Heat Trans* 128: 520–529, 2006.
20. **Huo Y, Li BQ.** Three-dimensional marangoni convection in electrostatically positioned droplets under microgravity. *Int J Heat Mass Trans* 47: 3533–3547, 2004.
21. **Kassab GS.** Functional hierarchy of coronary circulation: direct evidence of a structure-function relation. *Am J Physiol Heart Circ Physiol* 289: H2559–H2565, 2005.
22. **Kassab GS, Rider CA, Tang NJ, Fung YC.** Morphometry of pig coronary arterial trees. *Am J Physiol Heart Circ Physiol* 265: H350–H365, 1993.
23. **Kassab GS.** Scaling laws of vascular trees: of form and function. *Am J Physiol Heart Circ Physiol* 290: H894–H903, 2006.
24. **Kleinstreuer C, Hyun S, Buchanan JR Jr, Longest PW, Archie JP Jr, Truskey GA.** Hemodynamic parameters and early intimal thickening in branching blood vessels. *Crit Rev Biomed Eng* 29: 1–64, 2001.
25. **Ku DN.** Blood flow in arteries. *Annu Rev Fluid Mech* 29: 399–434, 1997.
26. **Ku DN, Gidden DP, Zarins CK, Glagov S.** Pulsatile flow and atherosclerosis in the human carotid bifurcation. *Arteriosclerosis* 5: 293–302, 1985.
27. **Lei M, Kleinstreuer C, Truskey GA.** A focal stress gradient-dependent mass transfer mechanism for atherogenesis in branching arteries. *Med Eng Phys* 18: 326–332, 1996.
28. **Lu X, Kassab GS.** Nitric oxide is significantly reduced in ex vivo pig arteries during reverse flow because of increased superoxide production. *J Physiol* 561: 575–582, 2004.
29. **Malek AM, Alper SL, Izumo S.** Hemodynamic shear stress, and its role in atherosclerosis. *JAMA* 282: 2035–2042, 1999.
30. **Moore JE, Xu C, Glagov S, Zarins GK, Ku DN.** Fluid wall shear stress measurements in a model of the human abdominal aorta: oscillatory behavior and relationship to atherosclerosis. *Atherosclerosis* 110: 225–240, 1994.
31. **Panton RL.** *Incompressible Flow*. New York; Wiley, 1984.
32. **Pedley TJ.** *The Fluid Mechanics of Large Blood Vessels*. Cambridge, UK: Cambridge Univ. Press, 1980.
33. **Perktold K, Resch M, Florian H.** Pulsatile non-Newtonian flow characteristics in a three-dimensional human carotid bifurcation model. *J Biomech Eng* 113: 464–475, 1991.
34. **Perktold K, Resch M, Peter RO.** Three dimensional numerical analysis of pulsatile flow and wall shear stress in the carotid artery bifurcation. *J Biomech* 24: 409–420, 1991.
35. **Ramaswamy SD, Vigmostad SC, Wahle A, Lia YG, Olszewski ME, Braddy KC, Brennan TMH, Rossen JD, Sonka M, Chandran KB.** Fluid dynamics in a human left anterior descending coronary artery with arterial motion. *Ann Biomed Eng* 32: 1628–1641, 2004.
36. **Sankaranarayanan M, Ghista DN, Poh CL, Seng TY, Kassab GS.** Analysis of blood flow in an out-of-plane CABG model. *Am J Physiol Heart Circ Physiol* 291: H283–H295, 2006.
37. **Stary HC, Blankenhorn DH, Chandler AB, Glagov S, Insull W Jr, Richardson M, Rosenfeld ME, Schaffer SA, Schwartz CJ, Wagner WD, Wissler RW.** A definition of the intima of human arteries and of its atherosclerosis-prone regions: a report from the Committee on Vascular Lesions of the Council on Arteriosclerosis, American Heart Association. Special report. *Circulation* 85: 391–405, 1992.
38. **Stary HC, Chandler AB, Dinsmore RE, Fuster V, Glagov S, Insull W Jr, Rosenfeld ME, Schwartz CJ, Wagner WD, Wissler RW.** A definition of advanced types of atherosclerotic lesions and a histological classification of atherosclerosis. A report from the Committee on Vascular Lesions of the Council on Arteriosclerosis, American Heart Association. *Circulation* 92: 1355–1374, 1995.
39. **Stroud JS, Berger SA, Saloner D.** Numerical analysis of flow through a severely stenotic carotid artery bifurcation. *J Biomech Eng* 124: 9–20, 2002.
40. **Taylor CA, Hughes TJR, Zarins CK.** Finite element modeling of three-dimensional pulsatile flow in the abdominal aorta: relevance to atherosclerosis. *Ann Biomed Eng* 26: 975–987, 1998.
41. **Tomochika Y, Tanaka N, Wasaki Y, Shimizu H, Hiro J, Takahashi T, Tone T, Matsuzaki H, Okada K, Matsuzaki M.** Assessment of flow profile of left anterior descending coronary artery in hypertrophic cardiomyopathy by transesophageal echocardiography. *Am J Cardiol* 72: 1425–1430, 1993.
42. **Traub O, Berk BC.** Laminar shear stress mechanisms by which endothelial cells transduce an atheroprotective force. *Arterioscler Thromb Vasc Biol* 18: 677–685, 1998.
43. **White CR, Haidekker M, Bao X, Frangos JA.** Temporal gradients in shear, but not spatial gradients, stimulate endothelial cell proliferation. *Circulation* 103: 2508–2513, 2001.
44. **Zarins CK, Giddens DP, Bharadvaj BK, Sottiurai VS, Mabon RF, Glagov S.** Carotid bifurcation atherosclerosis: quantitative correlation of plaque localization with flow velocity profiles and wall shear stress. *Circ Res* 53: 502–514, 1983.
45. **Zeindler CM, Kratky RG, Roach MR.** Quantitative measurements of early atherosclerotic lesions on rabbit aortae from vascular casts. *Atherosclerosis* 76: 245–255, 1989.
46. **Zeng D, Ding Z, Friedman MH, Ethier CR.** Effect of cardiac motion on right coronary artery hemodynamics. *Ann Biomed Eng* 31: 420–429, 2003.